UNIVERSITY OF BIRMINGHAM

University of Birmingham
Research at Birmingham

A comprehensive material and experimental investigation of a packed bed latent heat storage system based on waste foundry sand

Ahmad, Abdalqader; Anagnostopoulos, Argyrios; Navarro, M. Elena; Maksum, Yelaman; Sharma, Shivangi; Ding, Yulong

Document Version
Publisher's PDF, also known as Version of record

[Link to publication on Research at Birmingham portal](#)

A comprehensive material and experimental investigation of a packed bed latent heat storage system based on waste foundry sand

Abdalqader Ahmad [a], Argyrios Anagnostopoulos [a,b,c,*], M. Elena Navarro [a,**], Yelaman Maksum [a], Shivangi Sharma [a], Yulong Ding [a]

[a] Birmingham Centre for Energy Storage & School of Chemical Engineering, University of Birmingham, Birmingham, B15 2TT, United Kingdom
[b] Department of Mechanical Engineering, Aristotle University of Thessaloniki, PO Box 454, 54124, Thessaloniki, Greece
[c] Institute of Chemistry, University of Silesia, 40-006, Katowice, Poland

ARTICLE INFO

ABSTRACT

The EU's industrial sector discards about 18.9% of its energy as waste heat, much of which has the potential for recovery. This study addresses the challenge by focusing on the advancement of latent heat thermal energy storage (LHTES) using phase change materials (PCMs) encapsulated within industrial waste foundry sand (WFS). WFS, a problematic by-product, is repurposed as a supportive matrix for $NaNO_3$ and solar salt PCMs, tailored for effective integration into high-temperature industrial processes. The paper provides a thorough mechanical and thermal examination of the WFS-salt PCMs, highlighting their improved thermal stability, performance, and compatibility with direct thermal energy systems. The composite PCMs demonstrated melting points well-suited for industrial waste heat applications and achieved an energy density of 542.0 ± 8.3 kJ/kg for $NaNO_3$ and 516.0 ± 4.5 kJ/kg for solar salt, An experimental cascade PBLHS, based on these CPCMs, with a capacity of 262 MJ, designed to mimic an industrial heat source at 450 °C, was systematically tested to assess its energy density and efficiency over repeated charging/discharging and free cooling cycles. Its overall system efficiency is found to be 68.5%. These findings position WFS-salt PCMs as a promising and environmentally beneficial approach to enhance industrial energy efficiency and utilisation.

1. Introduction

The foundation industries underpin many aspects of our economy and are also among the most challenging sectors to decarbonise in a sustainable manner [1]. The EU has set an ambitious target of a 42 % reduction in industrial sector carbon emissions by 2030 [2]. As per an EU estimate, the industrial sector accounts for 27 % of the overall energy consumption and the generation of 30 % of heat-related CO_2 emissions [3]. Industrial thermal processes account for 70 % of the energy demand, which is equivalent to 18.9% of the total EU energy demand [4]. Thermal processes emit a large amount of waste heat with almost one-fifth (~400 TWh/yr.) being classified as high-grade, hence with good potential for recovery and reuse [5].

Waste heat recovery (WHR) is, thus among, the next frontiers for energy-intensive industries [6]. Among the available WHR technologies, thermal energy storage (TES) has the potential to solve the

discontinuous waste heat supply and heat demand mismatch problem [7]. TES can thus overcome the issue of temporal and geographical mismatch faced by technologies such as recuperators, regenerators, and heat pipes. Its flexible design adjusts the process components to lower maximum output, avoiding start-up and partial load losses [7]. This reduces capital investment compared to other WHR technologies, such as thermoelectric generators or Organic Rankine Cycle engines, making it a cost-effective solution to energy efficiency problems [8].

TES is broadly classified into sensible, latent, and thermochemical; the third is still at a material development stage in the medium to high temperature settings [9]. Sensible TES (STES) is a mature technology that uses inexpensive materials and has been applied on a large scale for hundreds of years but it exhibits low energy density and quick temperature drops during discharge [9]. Latent heat TES (LHTES), is centred on the ability of a material, commonly referred to as the phase change material (PCM), to absorb/release heat isothermally during its transition

---

from one state to another. It has been extensively investigated in recent years, and large-scale industrial deployments have been reported for peak electricity grids, solar energy utilisation, and waste heat recovery [10]. It displays minor temperature fluctuation during charging/discharging and has a higher energy density than STES [10]. However, PCMs suffer from disadvantages such as poor thermal conductivity, volume expansion, corrosion, and subcooling [11]. These affect the performance of LHTES at both the device and system levels but can be largely resolved by encompassing them in a porous matrix, typically consisting of refractory materials [12,13]. The resulting materials are called composite phase change materials (CPCMs). CPCMs, aside from LHTES, can also be effectively applied in combined STES-LHTES systems. Such hybrid TES systems have been shown to be extremely promising alternatives [14].

Waste foundry sand (WFS) is a by-product/waste from casting processes in the ferrous and non-ferrous metal casting industries. In a typical casting process, fresh sand is used to construct moulds in which the metal is poured in the desired shape. After solidification, the metal is extracted, and the sand is reused. Several approaches have been followed to recycle the sand internally in the foundries, reaching an average internal recycling rate of up to 80–98 %. However, this recycled sand can only be used for a finite number of casting cycles until the quality standards are being met, after which fresh sand is introduced into the mould. This massive surplus of sand is disposed of in landfills as metal casting necessitates large volumes of sand that cannot be accommodated in foundry warehouses [15]. WFS disposal is expensive due to increased transportation costs and high landfill taxes [16]. A 2020 survey by the Cast Metal Federation (CMF, UK) found that it accounts for 4 % of the annual turnover of an average sand foundry. China, India, and the USA are the world's largest producers of WFS, with a combined total of roughly 71 million tonnes [17]. A small fraction of WFS has found applications in concrete production, low-strength controlled materials, and road pavement materials [18]. Other novel proposed strategies include its use as a ground barrier against wet leakage from landfill sites and as a structural constituent in organic waste. However, the utilisation rate of WFS is still low [19].

The chemical composition of WFS (ceramic), density, particle size (0.15 mm $<D<$ 0.6 mm), and specific surface area make it a fairly good candidate as a supporting material for a CPCM [19]. This work focuses on CPCM for the medium-to-high-temperature range ($>200\,°C$). Streams at these temperatures are commonly present in foundation industries [20]. This provides a novel utilisation pathway for recycling the WFS as a key material for CPCMs for capturing, storing, and reusing waste heat.

As discussed, the encapsulation of PCMs is an effective method to enhance the charging/discharging performance [11]. This method can expand the heat transfer area and solve the leakage problem of the PCM. Furthermore, it enables the use of PCMs in direct heat transfer systems [21]. Direct TES systems have a lower thermal resistance due to the absence of an intermediate heat exchanger, hence, higher heat transfer characteristics [14]. Additionally, since the heat transfer fluid can also act as the storage medium during idle periods, the storage tank can be designed to benefit from the favourable thermal stratification, resulting in an improved system performance [14]. This indirectly improves the exergy of a system, particularly when idle state is involved [22]. Additionally, direct systems typically require less components than indirect systems and as such require less capital cost [23].

A popular direct TES system is the packed bed. Packed beds containing CPCMs are called packed bed latent heat storage systems (PBLHS). PBLHS are a simple and efficient technology which can be used in a wide temperature range as it can be incorporated with low temperature solar thermal applications or waste heat streams, as well as high temperature solar thermal applications such as concentrated solar power plants (CSP) and waste heat streams from steel mill exhausts [22]. Its wide application range, good overall efficiency and low capital cost have resulted in increased attention in PBLHS [24].

Early theoretical investigations of PHLHS date back to the late 1980s.

Ananthanarayanan et al. developed a computer model to predict the heat exchange phenomenon in a packed bed with encapsulated Al–Si PCMs, enabling its efficient use as a near-isothermal heat recuperator [25]. Around the same time, Beaslery and Ramanarayanan conducted one of the earliest experimental investigations of a PHLHS consisting of a bed with encapsulated paraffin wax. The authors studied the effective heat transfer coefficient over a range of Reynolds numbers [26]. Another early experimental work was conducted by Yagi and Akiyama on PBLHS with encapsulated metals for WHR applications at 500K [27]. More recently, Ismail and Henríquez developed a one-dimensional model of a PHLHS [14]. It handles capsule solidification with a conductive phase change model, accounts for liquid PCM convection via an effective heat conduction coefficient, and explores the system parameters' impact on charge/discharge times [28]. Nalusamy et al. explored the thermal behaviour of a combined STES-LHTES unit. The unit uses paraffin-filled capsules and water as the HTF. Experiments measured the impact of the inlet temperature, HTF flow rate, and the heat recovery methods. The authors found that the combined system performed better than the conventional ones for intermittent use [29]. Regin et al. analysed a PHLHS containing paraffin wax-filled capsules for a solar water heating setup. Using an enthalpy method to account for phase changes, they evaluated the effects of the inlet fluid temperature, flow rate, and the phase change temperature range on the system performance. They emphasized the importance of accurately knowing the PCM melting point for effective system modelling [21].

The issue is that most studies in PBLHS involved low temperature PCMs. Studies involving molten salts have only recently emerged in the last decade. Peng et al. investigated a PBLHS with molten salt capsules. Through finite-difference analysis, they explored the influence of the capsule diameter, fluid velocity, and the storage height on the temperature profiles and the charge efficiency. Their findings suggest optimizing these factors can enhance charge efficiency. In another work, Wu et al. assessed a molten-salt PBLHS, highlighting a quasi-isothermal period during discharge. They found that altering the PCM's melting point, the inlet velocity, and capsule diameter could improve the discharging efficiency [30]. The first experimental analysis of a molten salt PBLHS was conducted by Bellan et al. The authors examined the thermal performance of a TES system packed with sodium nitrate PCM-encapsulated capsules, utilizing air as an HTF. They validated, based on their experimental setup, a transient two-dimensional model. Using the model they highlighted the influence of factors such as the mass flow rate, Stefan number, and the shell properties on the system's thermal performance [31]. Bhagat and Saha modelled a PBLHS integrated into an ORC-based solar power plant. They found that a higher mass flow rate and high inlet charging temperature improved the performance. A decreased porosity effectively reduced HTF temperature variation, aiding in efficient system design [32]. Wu et al. modelled a cascaded PBLHS and found that cascaded systems outperformed the non-cascaded ones in terms of charging ratios and time. Especially those with 5 cascaded PCMs, had quick charge/discharge rates and yielded high efficiencies once a repeatable state was reached [33]. Zhao et al. analysed a molten-salt packed-bed TES systems in CSP, assessing the 'partial charge effect' and its impact on the thermocline and the energy storage/release. Their findings suggest that encapsulated PCM configurations are more resilient to these effects [34]. In a follow-up work, the authors conducted an optimization of the cut-off temperatures. Higher charging and lower discharging temperatures can boost efficiency, though deeper charges may increase pump requirements. They showcased the importance of optimal charging temperatures on cost-effectiveness [35]. Li et al. investigated experimentally a PBLHS, consisting of a 0.03 m³ tank, using a ternary carbonate mixture as PCM, which exhibited an energy density of 174.7 kJ/kg. They found that raising the inlet temperature and fluid mass flow rate boosted the system's efficiency. Through a validated model, they suggested that smaller capsule diameters can optimize the performance. Their system outperformed a shell and tube system in charging rates and overall

efficiency [36]. Liao et al. simulated the melting process of $NaNO_3$ in a spherical capsule via a natural convection-inclusive model and proposed a new effective thermal conductivity correlation for improved PBLHS modelling [37]. Liu et al. developed a 3D model of a PBLHS and revealed that radial porosity variations affect PCM melting and heat transfer. They also suggested that higher aspect ratios improve the system efficiency, despite an increased pressure drop [38]. Li et al. investigated a PBLHS with a carbonate ternary as the PCM. The authors, using a validated CFD model, showed that the CPCM TES outperforms a sensible system due to superior storage density and conductivity. Adjusting Reynolds and Stefan numbers, and adding graphite to the CPCM can further optimize the charge/discharge rates [39]. Saha and Das investigated numerically the performance of a PBLHS based on encapsulated molten carbonate ternary. They found that a two layer PBLHS showed superior charging efficiency especially at lower HTF flow rates, but a slightly reduced second law efficiency [40]. Yang et al. studied a PBLHS via simulations and experiments using a 0.01 m^3 tank. They found that thermocline thickness decreases with rising volume heat capacity but increases over time. The particle's equivalent diameter had negligible effect on the thermocline thickness, while porosity indirectly influenced it. They also observed a decreasing maximum temperature difference between the fluid and solid over time, while the range of these differences increased [41]. Wang et al. developed a transient two-dimensional dispersion-concentric model to model a PBLHS. Results showed that the radial gradient arrangement significantly enhances the heat transfer performance and reduces the system pressure drop with a maximum overall energy efficiency of 84.16 % [42]. Sau et al. explored a PBLHS with a cost-effective chloride-carbonate eutectic PCM. A realistic storage efficiency of 0.6 was attained using air as the HTF. The estimated investment cost ranges from 25 to 40 EUR/kWh, indicating potential economic benefits [43]. Nekoonam and Ghasempour developed a 2-D model to analyse a solar integrated PBLHS with molten salt as PCM and synthetic oil as HTF. The authors, optimized the thermal conductivity of the PCM through a Genetic Algorithm (GA). Adjustments in the input HTF temperature and the flow rate significantly influenced the charging time and the stored energy [44]. Erregueragui et al. conducted a technoeconomic evaluation of a PBLHS for a 100-MW power plant scenario with a 6 h of backup. Their findings suggested that cost could be reduced to up to $9/kWh with specific enhancements [45]. El Sihy et al. investigated numerically a PBLHS in terms of number of PCMs and their arrangement, latent heat, and capsule sizes with respect to the system performance. Their results highlighted an improved performance with certain PCM configurations, a significant impact of latent heat, and superior behaviour with smaller capsule sizes [46]. Wang et al. constructed an experimental PBLHS, using a 0.013 m^3 tank, using binary nitrate as the PCM, studying its heat transfer characteristics during charging, heat preservation, and discharging processes. They found the temperature difference inside the storage tank first increased, then decreased, stabilizing at about 84 °C when the average air temperature was 225–272 °C. Their results also revealed significant effects of the air temperature and the flow rate on the system pressure loss. The overall efficiency of their PBLHS system was 79.3% [47]. Manente et al. developed an algorithm to enhance heat recovery from a steel industry's flue gas, focusing on steam or electricity production. They found that a PBLHS, in combination with organic Rankine or Kalina cycles, produced the most steam and electricity. The investment had a payback period of seven years, making it more profitable than the high-cost tank-based storage units [48]. He et al. proposed an optimized two-layered PBLHS consisting of a 0.05 m^3 tank, considering PCM melting temperature, capsule diameter, and filling volume ratio. Detailed experimental results highlighted a temperature gradient that improved heat transfer efficiency and a superior overall efficiency in the optimized system compared to single-size PCM capsules. Optimal thermal performance and exergy efficiency were achieved at a specific volume filling rate of 1/2 [49].

Conclusively, a thorough review of the relevant literature reveals

that the majority of the research conducted on PBLHS involving molten salts largely focus on numerical simulations and techno-economic analyses, primarily targeting the optimization of individual design parameters. Unfortunately, there is a scarcity of experimental data, with only a handful of studies offering empirical insights. Most of these investigations involve laboratory-scale studies, utilizing tank sizes that measure in the order of millimetres, thus failing to emulate realistic application conditions for effective heat capture. Additionally, a significant number of these studies resort to using PCMs encapsulated in metallic capsules, a choice that comes with considerable expense.

In stark contrast to the existing research, this work introduces an innovative CPCM derived from WFS. It successfully demonstrates its potential for reutilization within a PBLHS system, employing a tank that is nearly ten times larger than those typically reported in the literature. This scale is pertinent for industrial WHR applications, thereby offering a viable, cost-effective solution that aligns more closely with the real-world conditions. By utilizing WFS as a base for the proposed CPCM, an otherwise discarded material is repurposed, which effectively integrated waste management with advanced TES solutions, hence promoting circular economy and fostering a greener, more sustainable future in the field of industrial heat and material recovery. The versatility and adaptability of this technology, make it beneficial for various weather conditions, including cold and arid areas where heat is most needed. However, to effectively apply it in such climates, it is crucial to optimize the CPCM properties accordingly and ensure the system is very well insulated. Notably, this technology is not limited to WHR applications but can be also used in direct thermal energy systems, particularly in combination with mobile TES, to extract and deliver heat from renewable energy sources, such as geothermal or solar, to provide targeted heating or cooling in various industrial, commercial, or residential settings, irrespective of their permanent energy infrastructure.

2. Materials and methods

2.1. Material formulation

The goal of this research is to provide an alternative utilisation pathway for WFS. To this end, WFS is used as the skeleton material and molten nitrate salts as the PCM and MgO as a supporting material The latter, has been extensively investigated in the literature and its chemical and physical compatibility with molten salt PCMs is well known. In fact, Nanjing Jinhe Energy Material Co., Ltd, is currently investigating the pilot-scale production of CPCMs based entirely on MgO, with a focus on salt-PCMs [50]. For the fabrication of the CPCMs, the sand, MgO and the salt grains are mixed at the desired mass ratio and then milled in a ceramic mortar. Water is then added, at 5 wt % and the mixture is then stir-hand-mixed to obtain a homogenous mix. It is then compressed at 28 MPa for 1 min, in a 15 mm diameter pellet compression dye. The produced pellet is then placed into an electric furnace (HTF 18/27, Carbolite, UK). It is heated at 80 °C with a heating rate of 5 °C/min and maintained there for 3 h to slowly evaporate the moisture in the mixture. This is followed by heating up to 400 °C (5 °C/min) followed by natural cooling down to ambient temperatures to produce the final shape-stable sintered pellets.

The composition of the CPCMs was WFS-MgO-PCM at a 0.4-0.2-0.4 mass ratio. Lower contents of MgO or higher contents of WFS or PCM resulted in material instability due to the non-cohesive nature of the sand grains, which is further amplified in WFS due to the sintered sand grains having a lower mean particle size [19]. The shape of the manufactured CPCM pellets was cylindrical and their dimensions were 60 ± 0.2 mm diameter and 50 ± 0.25 mm height. The average mass of the pellets was 222.66 ± 8.25g for the SS and 220.70 ± 10.60g for the ones containing $NaNO_3$.

A temperature gradient is typically observed during the charging and discharging of TES systems. In fact, long timescales are necessary for a TES device to reach the temperature equilibration. To this end, in order

to maximize the storage capacity, a cascade system was envisaged. This contains two PCMs with different melting points NaNO$_3$ with a melting point at 308 °C and Solar Salt (SS), a commonly used PCM in the CSP industry (Fig. 1). The latter is essentially a mixture of NaNO$_3$ and KNO$_3$ with a 0.6–0.4 mass ratio. The PCM used in this work (NaNO$_3$ and KNO$_3$) were purchased from Sigma-Aldrich at a chemical grade purity (>99.9%). MgO was purchased from VWR International Limited.

The WFS was obtained from "Boro Foundry", a West Midlands (UK) based specialist manufacturer-supplier of a wide range of castings and machine parts using a variety of ferrous and non-ferrous metals.

2.2. Material Characterization

The grain density of the sand is measured using a helium pycnometer (Accupyc II 1340, Micromeritics) which was found to be 2.51 ± 0.06 g/cm^3. The bulk density of the fabricated CPCMs is measured by obtaining the respective pellet's mass and dimensions (volume). The porosity of the CPCM is then calculated using the density ratio.

To characterize the specific heat capacity, latent heat, and the thermal diffusivity of the samples, manufactured pucks of the two different CPCM compositions were crushed and milled after being heat treated. The homogeneous powder was then tested for specific heat capacity and pressed into 12.7 mm pellets for thermal diffusivity.

Differential Scanning Calorimetry (DSC) is employed to measure the melting point, latent heat, and specific heat capacity of the samples. Measurements are carried out in a DSC3 Mettler Toledo from 20 to 400 °C with a heating rate of 10 °C/min in aluminium crucibles under air atmosphere. Specific heat measurements are obtained according to DIN51007 standards and following the sapphire method [51]. To mitigate the high error associated with Differential Scanning Calorimetry (DSC), the samples were introduced into the crucibles as 5 mm diameter pellets, with uniform mass and compression rates analogous to the CPCMs.

Thermal diffusivity and thermal conductivity are obtained by the Laser Flash Analyser Technique (LFA) with an LFA 427 device (Netzsch). The surface of the samples is flattened to obtain parallel surfaces and then coated with a graphite layer, which helps prevent the direct transition of the laser beams and helps the energy transfer of the sample. The test is performed under a 100 ml/min airflow condition. The thermal conductivity is then calculated through the following equation (1):

$$\lambda = a(T)\rho(T)C_p(T) \tag{1}$$

where, T is temperature (K), α is thermal diffusivity (mm^2/s), ρ is density (g/cm^3) and C$_p$ is heat capacity (J/gK).

Compressive strength is measured using a universal mechanical testing machine (LS100, Lloyd Instruments Co., Ltd., UK). Test are performed until breakage (rupture) by applying constant load. The elastic modulus is then obtained using the following relationship:
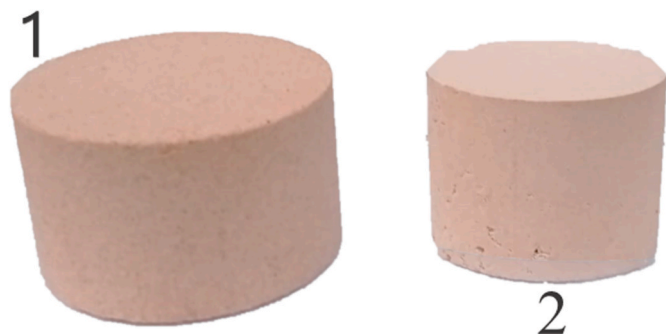

Fig. 1. Fabricated CPCM pellets after thermal cycling: Containing NaNO$_3$ (1) and Solar Salt (2).

$$E = \frac{\Delta H}{H}\Delta\sigma \tag{2}$$

where, E is the elastic modulus (MPa), H the sample height (m), ΔH the change in sample height from the start of compression until breakage (g/cm^3) and $\Delta\sigma$ the compressive strength (MPa).

The thermal cycling protocol consisted of a heating step up to 400 °C, an isothermal step at 400 °C for 12 h, and a cooling step down to ambient, followed by an isothermal hold at that temperature for 1 h. The samples underwent a total of 20 cycles.

2.3. Experimental setup

The main objective of this work is to develop a PBLHS unit based on WFS-CPCMs. The system is tasked at capturing and reusing the industrial waste heat. Within waste heat from industrial gases, there is a wide range of heat source temperatures. Among them, there is a high number of streams with temperatures between 200 and 450 °C such as kiln exhaust gases in the cement industry, rolling mills and soaking pits in the steel industry, flat glass in the glass industry, gas turbines in the chemical and internal combustion engines [20]. This high availability of industrial waste heat serves as a good opportunity for showcasing a use case of a PBLHS-TES.

To this end, a 10 kW energy source is selected to emulate a waste heat source of this temperature range. The, 10 kW electric outlet is coupled with a heating element in the form of an open cross-shaped spiral (Fig. 2). This configuration is an optimal choice for air preheaters, particularly due to its shape, which maximizes heat transfer, making it suitable for delivering the high temperatures required in this case. The spiral measures 390 mm in length and was installed within a 590 mm tube having a diameter identical to the tank inlet. The tube was mounted on the top of the tank and connected to a fan. The fan is a high-temperature specialized VOK series model from MMotors SA, designed to operate up to 150 °C (Fig. 2). The air coming through the fan is in ambient temperature. To avoid any potential overheating issues due to losses from the tank or in the form of backflow, a model that can withstand slightly higher temperatures than ambient was selected. The fan's body, turbine, and back shutter are all from an aluminium alloy. Both the fan and the heating element are connected to a PID controller box.

The tank system was originally envisaged as a four-stage cascaded system with different PCMs. However, due to budget limitations only one tank was kept. In theory, one tank is sufficient to evaluate the performance of a four-tank system, as one can determine the efficiency of one unit and extrapolate that to a larger system [52], assuming that the geometry of all four tanks would be identical [53].

The tank has a diameter of 628 mm and a height of 2010 mm. The packed bed section is 1600 mm long. This results in an aspect ratio of 2.5. Higher values were limited by tank structural constrains as well as the height of the hangar.

Utilizing the specific heat capacity and density values, the energy storage density for the NaNO$_3$ and SS-based CPCMs was determined to be 542.0 ± 8.3 kJ/kg and 516.0 ± 4.5 kJ/kg, respectively. Given the standardized dimensions of the pellets provided by the manufacturing company, which were 50 mm in diameter and 60 mm in height, the porosity in the packed bed arrangement was calculated using a formula provided by Benyahia and O'Neil, who developed a fit based on the geometry and aspect ratio of materials and validated it using experimental data [54]. The porosity was estimated to be 36%. This resulted in a total of 2230 CPCM pucks.

However, upon evaluation, the mechanical stability of the CPCMs, was found to be poor (see section 3.1). In response to this, a series of metal sieve trays along with a 12-inch metal rod were procured. A stack of 26 trays was assembled and secured to a central metal rod. The pellets were then loaded onto each tray (Fig. 3), with a total of 76 pellets per
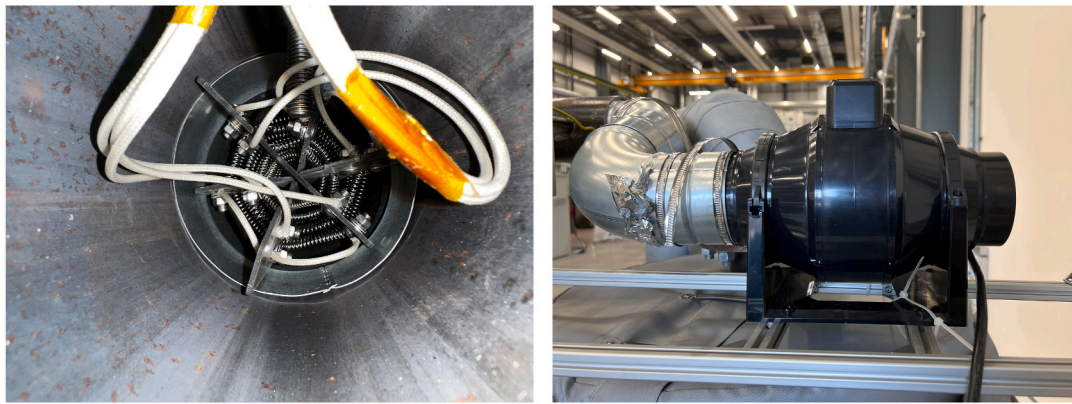
Fig. 2. Left: Cross-shape spiral heating element; Right: VOK series fan from MMotors SA mounted.

Fig. 3. Left: Tank trays with pellets loaded in the tank using a lift crane. Right: Stack of pellet covered trays half covered with aluminium foil.

tray. A small gap was left between pellets to accommodate for the thermal expansion. This amounted to a total of 1976 pellets, resulting in a tank porosity of 48 % when considering the volume of the trays. Of these 1712 are filled with SS and 264 with $NaNO_3$. The $NaNO_3$ containing pellets are positioned at the top layers of the tank given their higher melting point. This brings the total energy capacity of the system, including the trays, to approximately 262 MJ. To facilitate loading and prevent potential issues arising from the differing thermal expansion of the two steel alloys, the trays were designed with a diameter 2 cm smaller than that of the tank. To counteract the resulting gap, which could have diverted the air flow from the centre of the tank where the rod and pellets were positioned, the stack of trays was enclosed within an aluminium cylindrical sieve of a larger diameter (Fig. 3).

The total weight of the trays and pellets exceeded 600 kg. With the aid of a lift crane, this structure was loaded into the tank (Fig. 3). There remained enough space in the tank for an additional 6 trays. While this could have increased the solid fraction and decreased porosity to 28 %, the inclusion of the stainless steel trays had brought the total load precariously close to the structural limit of the tank. The total tank load of 840 kg, coupled with the elevated operational temperatures, which induce additional stress, raised stability concerns. Furthermore, a higher porosity results in an increase in pressure drop, which is not beneficial for the charging/discharging efficiency of the TES device. A trade-off between efficiency and energy density is necessary in each case depending on the particular conditions of each heat stream.

After filling the tank, it was sealed and insulated with Siltherm Quilt, a flexible microporous insulation panel purchased from Siltherm. This insulation choice was ideal for the operating temperature range of the system given its relatively low average thermal conductivity (0.024 W/mK) and light nominal density (220 kg/m^3).

Based on the company's calculations (Siltherm), a 40 mm thickness of insulation was chosen for the tank. A thicker layer did not significantly reduce heat loss, hence was not considered cost-effective. A thickness of 10 mm was deemed sufficient for insulating the pipes and elbows. The insulation was conveniently fitted and easy to assemble, fastened onto the tank using reinforced wire springs provided by the company (Fig. 4).

Additionally, a set of 16 K-type thermocouples was procured and installed on the rig (Fig. 4). Two one-way valves were positioned at the inlet and outlet of the first and the second tanks respectively, oriented in the same direction.

A depiction of the insulated tanks fitted with the heating element, the thermocouples, and the fan is provided below (Fig. 4). Subsequently, the heating element was covered with the insulation provided by the company.

2.4. Performance analysis

In the process of energy absorption and release, the energy conveyed to the thermal reservoir and the energy extracted from the thermal reservoir by the HTL (Heat Transfer Liquid) are described as:
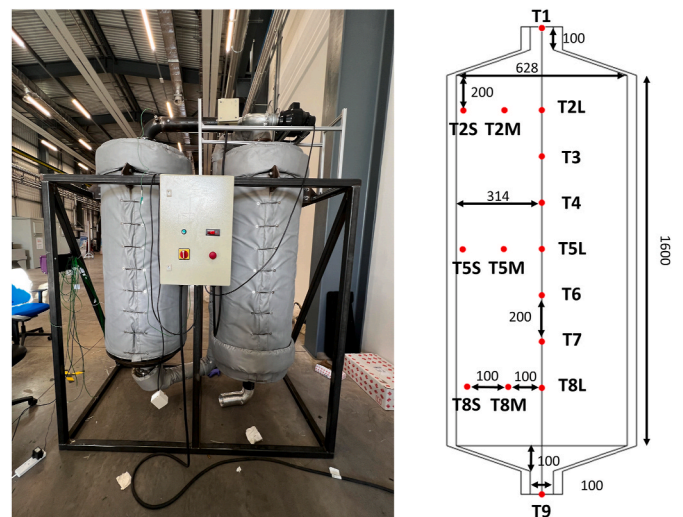

Fig. 4. Left: Final setup of the two insulated tanks. Thermocouples and data logger can be seen on the left. Control box in the centre is connected to the fan (top right), which is in line with the heater (black tube at the top). Right: Thermocouple positions in the tank. (dimensions in mm).

$$Q_{inflow} = m_{flow} \cdot \Delta t \cdot \sum_{i=1}^{n_{data}} \left(T_{entry,avg} \cdot C_{p,entry} - T_{exit,avg} \cdot C_{p,exit} \right) \tag{3}$$

and

$$Q_{outflow} = m_{flow} \cdot \Delta t \cdot \sum_{i=1}^{n_{data}} \left(T_{exit,avg} \cdot C_{p,exit} - T_{entry,avg} \cdot C_{p,entry} \right) \tag{4}$$

where, m_{flow} stands for the airflow rate; $T_{entry,avg}$ and $T_{exit,avg}$ represent the

mean temperatures of the air at entry and exit points respectively; $C_{p,entry}$ and, $C_{p,exit}$ signify the average specific heat capacities at the entry and exit points; Δt is the interval of time captured by the data recording device (30s); n_{data} symbolizes the count of data acquisition points.

The charging (η_{ch}) and discharging efficiency (η_{dis}) of the PBLHS is then denoted as:

$$\eta_{ch} = \frac{Q_{max}}{Q_{inflow}} \tag{5}$$

and

$$\eta_{dis} = \frac{Q_{outflow}}{Q_{max}} \tag{6}$$

where Q_{max} is the maximum theoretical energy that can be captured by the PBLHS. This encompasses three components: the energy retained by the CPCM, the energy retained by the carbon steel tank, and the energy retained by the HTF. Consequently, it can described as:

$$Q_{max} = Q_{tank} + Q_{HTF} + Q_{CPCM} \tag{7}$$

The energy retained by the tank, HTF and CPCM is then expressed respectively as:

$$Q_{tank} = m_{steel} C_{p,steel} \left(T_{entry,avg} - T_{init} \right) \tag{8}$$

and

$$Q_{HTF} = V_{flow} \rho_{flow} C_{p,flow} \left(T_{entry,avg} - T_{init} \right) \tag{9}$$

and

$$Q_{CPCM} = m_{CPCM} C_{p,solid} \left(T_{entry,avg} - T_m \right) + m_{CPCM} h_t + m_{CPCM} C_{p,liquid} \left(T_m - T_{CPCM,final} \right) \tag{10}$$

where, m_{steel} and m_{CPCM} is the total mass of the steel and CPCM respectively; T_{init} denoted the initial temperature; V_{flow} the flowrate of air; ρ_{flow} the density of air; T_m, and $T_{CPCM,final}$, denote the melting point temperature and the final temperature of the CPCM, respectively. $C_{p,solid}$ and $C_{p,liquid}$ denote the specific heat capacities of the solid and liquid phases of the CPCM, respectively, while $C_{p,steel}$ stands for the specific heat capacity of stainless steel; h_t the latent heat during solid liquid phase transition.

The energy density of the CPCM is then calculated as:

$$\epsilon_{mass} = \frac{Q_{CPCM}}{m_{CPCM}} \tag{11}$$

The thermophysical properties of the CPCM are obtained from experimental measurements. These of air are obtained as a function of temperature through correlations provided in the literature that are matching the operating conditions of the PBLHS presented here [55].

These are:
For the density:

$$\rho_f \left(kg/m^3 \right) = 7.487 \times 10^{-7} T_f^6 - 2.68 \times 10^{-13} T_f^5 + 3.898 \times 10^{-10} T_f^4 - 3.025 \times 10^{-7} T_f^3 + 0.0001421 T_f^2 - 0.04642 T_f + 12.81 \tag{12}$$

And for the specific heat capacity under constant pressure,

$$c_{pf}(J/kgK) = 3.756 \times 10^{-10} T_f^4 - 1.042 \times 10^{-6} T_f^3 + 0.0009458 T_f^2 - 0.1178 T_f + 1023 \tag{13}$$

The total efficiency (η_{total}) of the PBLHS is then determined as follows:

$$\eta_{total} = \eta_{ch} \cdot \eta_{dis} = \frac{Q_{inflow}}{Q_{outflow}} \tag{14}$$

Finally, the rate of energy absorption and release are described as:

$$P_{in} = \frac{Q_{inflow}}{\tau} \tag{15}$$

And

$$P_{out} = \frac{Q_{outflow}}{\tau} \tag{16}$$

where τ denotes the data logger's temperature recording interval.

2.5. Uncertainty analysis

The precision of experimental measurements invariably contains discrepancies stemming from the instruments used during the data collection process. For the PBLHS, the uncertainty in measurements arises primarily from the accuracy of the thermocouples, the flowmeter, and the data logger. The uncertainties associated with these devices, sourced from their respective manufacturer's specification sheets, are outlined in Table 1.

Knowing the uncertainty in the data collection process means the uncertainty on the performance variables can be evaluated. In line with the methodology proposed by Holman [56], consider a resulting uncertainty value S derived from multiple independent variables as:

$$S = S(Y_1, Y_2, Y_3, \ldots, Y_n) \tag{17}$$

Then the total uncertainty in an output can be described as:

$$\Delta S = \sqrt{ \left(\Delta Y_1 \frac{\partial S}{\partial Y_1} \right)^2 + \left(\Delta Y_2 \frac{\partial S}{\partial Y_2} \right)^2 + \ldots + \left(\Delta Y_n \frac{\partial S}{\partial Y_n} \right)^2 } \tag{18}$$

where, ΔY_1, ..., ΔY_n are the uncertainties associated with each independent variable Y_1, ..., Y_n respectively.

In the analysis, the uncertainties from the measurement devices, as listed in Table 1, were assigned to relevant independent performance variables, according to their respective equations. By employing partial

Table 1
Uncertainties associated with data measurement devices.

Experimental Device	Model Number	Uncertainty
Thermocouples	RS PRO Type K (NiCr -NI)	$\pm 0.004 \cdot T$
Flowmeter	ANNMETER AN-866A	$\pm 0.02 \cdot m$
Data Logger	Datataker DT85	$\pm 0.001 \cdot \Delta t$

Table 2
Uncertainties associated with performance analysis variables.

Parameter	Uncertainty
Energy Stored (Q_{inflow})	± 115 kJ
Enery Extracted (Q_{outflow})	± 89 kJ
Charging Efficiency (η_{ch})	$\pm 1.83\%$
Discharging Efficiency (η_{dis})	$\pm 2.31\%$
Total Efficiency (η_{total})	$\pm 2.11\%$

derivatives, the impact of each variable on performance metrics was assessed. Through equation (18), these individual uncertainties were combined to deduce the composite uncertainty for each parameter, which is detailed in Table 2.

3. Results and discussion

3.1. Material characterization results

Among the tested CPCMs, those containing Solar Salt (SS) and NaNO$_3$ (Na) exhibited comparable densities, with values of 1.89 ± 0.07 g/cm³ and 1.87 ± 0.09 g/cm³ respectively, as depicted in Fig. 5.

In Fig. 5a, the density for the SS pellets with respect to thermal evolution is illustrated. The density appears to be stable with further cycling. Similar behaviour was observed in the case of Na. This indicates that the structure is physically stable. With respect to porosity, the Na and the SS samples have a value of 32.5 and 33.8 % respectively. This is in agreement with what is typically reported for such samples in the literature [11]. Porosity is expected in CPCMs as the matrix needs to accommodate for the high-volume change of the PCM during phase transition (9.7 ± 0.5 %) as well as the differences in the thermal expansion coefficient of liquid and solid [57].

The specific heat capacity (C_p) is an essential property for CPCM performance in TES systems. For the examined materials it was determined across a temperature range of 0–500 °C, (Fig. 6a). The CPCM consisting of SS molten salt showcased a prominent rise in C_p, from an initial value of approximately 1.06 J/gK to nearly 1.33 J/gK, when the temperature was elevated from 0 °C to around 200 °C, nearing its phase change temperature. Beyond this phase transition, the C_p of SS samples seems to stabilize around 1.33 J/gK, with only minor fluctuations observed up to 500 °C. Conversely, the CPCMs that contain NaNO$_3$ exhibit a different behaviour. Their C_p starts at roughly 1.10 J/gK at 25 °C and increases up to around 1.43 J/gK at 250 °C. This is followed by a gap around its phase transition temperature, which is approximately 308 °C. Post this phase change, the C_p levels off at about 1.40 J/gK and maintains this value up to 475 °C.

The presented data highlights the effects of molten salt phase transitions on their C_p values. Additionally, the mild increase in the C_p outside the phase transition regions may be associated with the slow release of trapped moisture within the composite. As this moisture evaporates, it absorbs a significant amount of heat, thereby increasing the overall heat capacity. This underlines the importance, yet complexity, of the initial drying process and the sample preparation, given that residual moisture can considerably alter the thermal measurements.

On aggregate, the SS CPCM presents a lower C_p pre and post phase transition compared to the NaNO$_3$ composite (1.09 versus 1.22, and 1.3 versus 1.35 J/gK). This finding is in alignment with the classical mixing theory since SS has a lower C_p than NaNO$_3$.

Regarding the latent heat of the CPCM composites, those incorporating NaNO$_3$ display higher latent heat values, with measured amounts of 39.0 ± 1.1 and 59.1 ± 2.6 J/g for SS and NaNO$_3$ samples, respectively (Fig. 6). This outcome aligns with the expectations, given that the latent heat of CPCMs is inherently tied to the latent heat of the PCMs, which stands at 108 and 173 J/g respectively [58]. However, a noteworthy observation is that both the types of the samples, and particularly those with NaNO$_3$, possess a significantly reduced latent heat compared to the values projected by the mixing theory (Fig. 6). This discrepancy could
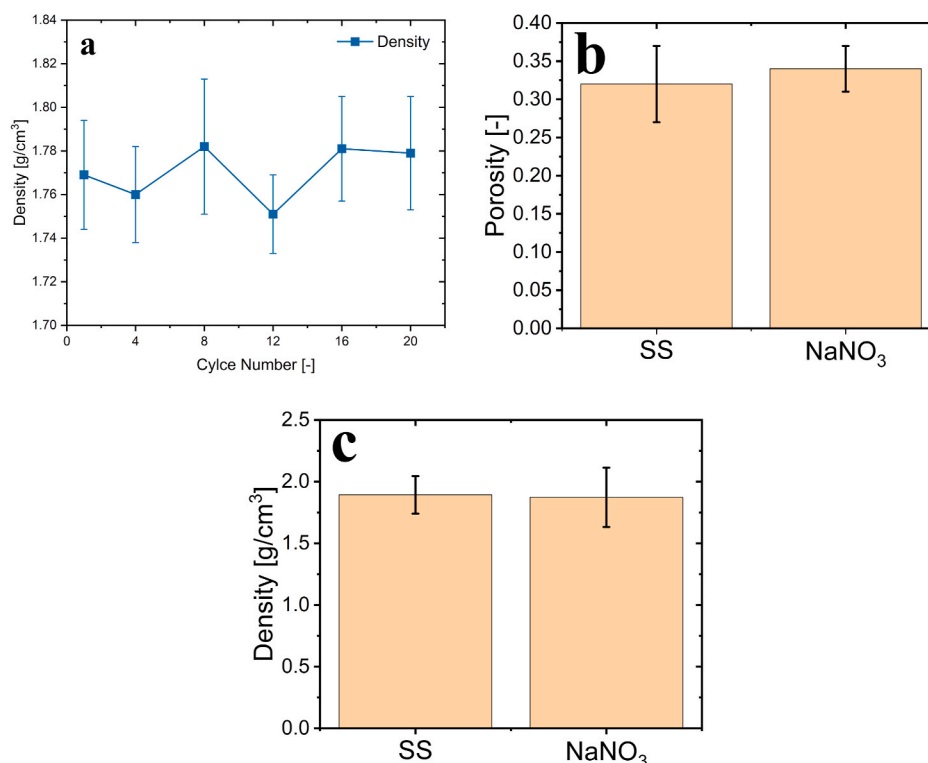

Fig. 5. a: SS Density evolution over cycling; b: Average sample Porosity; Bottom c: Average sample density.
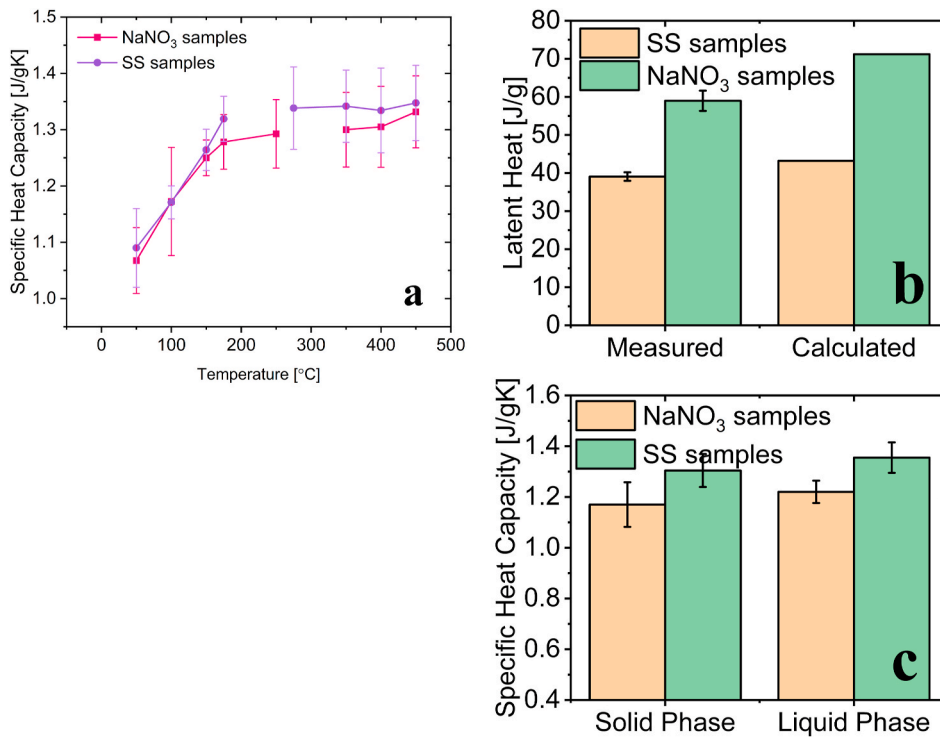
Fig. 6. a: Specific heat capacity versus temperature; b: Measured and calculated latent heat; c: Average C_p in liquid and solid phase.

potentially indicate some degree of leakage during the first stages of thermal cycling.

Furthermore, this reduction in enthalpy might be ascribed to the confinement of PCM during phase transition, a notion corroborated by previous research. For instance, Mitran observed this phenomenon in the context of a salt-SiO$_2$ CPCM, while Xu et al. reported an average decrease of 4.9 % in the latent heat of a NaNO$_3$-diatomite CPCM [59,60]. Such findings substantiate the complexities involved in the thermal behaviour of such composites and showcase the importance of understanding these nuances when estimating the energy density of CPCMs for practical applications.

The energy storage density of the investigated CPCMs is calculated using the specific heat capacity, the latent heat and the density data provided in the previous sections, in the temperature range of 25–450 °C. As anticipated, the samples containing NaNO$_3$ demonstrate a higher energy density, with values reaching 542.0 ± 8.3 kJ/kg or 1074 MJ/m^3. This is in comparison to the SS samples, which exhibited an

energy density of 516.0 ± 4.5 kJ/kg or 1117 MJ/m^3. The higher performance of the NaNO$_3$ samples can therefore be primarily attributed to their elevated density, latent heat, and specific heat capacity.

These findings are comparable to previous state-of-the-art research into NaNO$_3$/stone-sawing-mud CPCMs, which reported an energy density of only up to 444.86 kJ/kg [61]. This underscores the advanced performance capabilities of the investigated CPCMs and paves the way for their potential application in high-performance TES systems.

Thermal conductivity is a critical parameter in CPCM composition and design and significantly impacts the charging and discharging rate of a TES system. It governs the power capacity of the TES system and is influenced by various factors. In this study, the data spanned temperatures from 25 °C to 400 °C for the SS composite and 25 °C–500 °C for the NaNO$_3$ ones (Fig. 7).

The SS composite exhibits a decrease in thermal conductivity from 1.46 W/mK at 25 °C to 1.04 W/mK at 400 °C, averaging 1.17 ± 0.52 W/mK across the investigated temperature range. Similarly, the NaNO$_3$
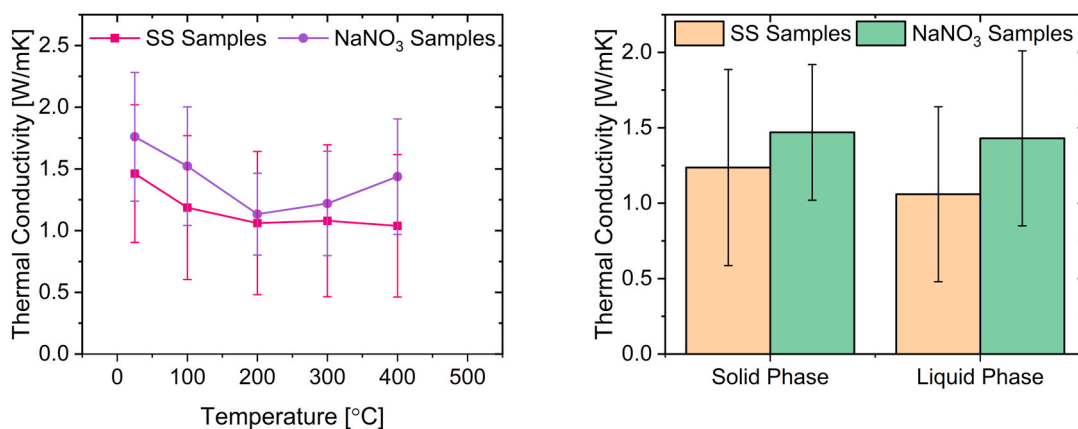

Fig. 7. Left: Thermal conductivity versus temperature; Right: Average thermal conductivity in solid (left) and liquid (right) phases, of the CPCMs investigated in this work.

composite records a decline from 1.76 W/mK at 25 °C to 1.48 W/mK at 400 °C, with a trough at 1.13 W/mK at 200 °C and an average of 1.45 ± 0.4 W/mK. Both the composites demonstrate an initial drop in the thermal conductivity with an increase in the temperature, followed by a plateau or minor increase. These behaviours are governed by the role of phonon scattering in ceramic materials like MgO, which intensifies with rising temperature and typically leads to a reduction in thermal conductivity [62]. Overall, the composites' data fall within the corresponding error margins for each temperature. For instance, at 300 °C, the thermal conductivity of the SS composite is 1.08 W/mK with an error of 0.715, while the NaNO$_3$–MgO composite displays 1.22 W/mK with an error of 0.523. The similarity in their thermal conductivities is expected, given the small difference in porosities (32.5 % for SS and 33.5 % for NaNO$_3$), and the similar intrinsic thermal conductivities of SS (0.51 W/mK) and NaNO$_3$ (0.50 W/mK) [63]. Notably, the encapsulation of the PCMs within ceramic matrices significantly enhances the thermal conductivity of the resulting TES materials.

As mentioned in Section 2.3, the mechanical behaviour of the CPCMs prompted the use of tray supports for their containment. This strategy was necessitated by the significant reduction in tensile strength that both tested composites displayed at temperatures above their respective salt's phase change points. Here, a detailed examination of this behaviour through the temperature versus the tensile strength measurements is presented.

For the SS composite, the tensile strength at the ambient temperature was 16.10 MPa (SD = 2.54), slightly increasing to 17.58 MPa (SD = 1.48) at 100 °C (Fig. 8). However, as the temperature approached and exceeded the phase change point of SS (220 °C), a substantial decline in the tensile strength occurred. At 200 °C, the tensile strength was recorded at 6.42 MPa (SD = 0.71), dropping further to 0.56 MPa (SD = 0.10) at 300 °C.

Similarly, the composite consisting of NaNO$_3$ displayed consistent tensile strength of 35.37 MPa at ambient temperature and 100 °C. This decreased to 25.95 MPa (SD = 7.62) at 200 °C. Beyond the phase change temperature of 308 °C, the tensile strength reduced drastically to 0.26 MPa (SD = 0.21) at 300 °C and 0.21 MPa (SD = 0.21) at 400 °C.

These considerable reductions in tensile strength beyond the salts' phase change points can be attributed to their transition from a solid to a liquid state within the composite, which negatively impacts the structural integrity and the mechanical stability of the materials due to the inherent lack of rigidity in the liquid state. Furthermore, upon phase change, the liquid state of the PCM also exhibits increased volume and a higher coefficient of thermal expansion. This expansion could introduce additional stresses within closed pores where the PCM is confined, further challenging the integrity of the solid skeleton of the composite.
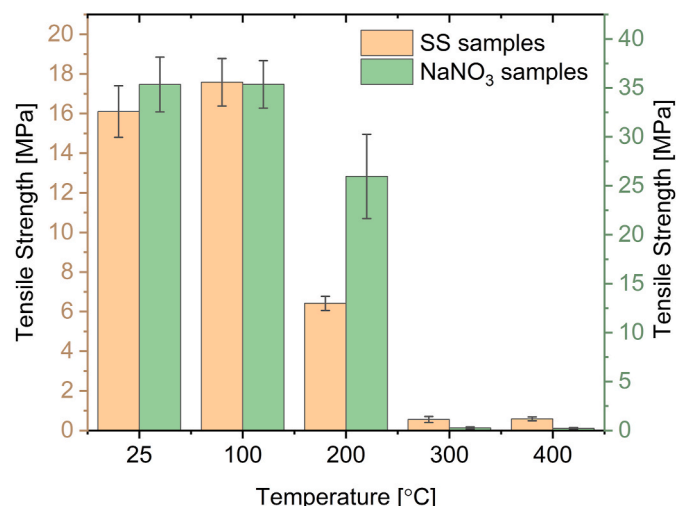

Fig. 8. Tensile strength of the CPCMs investigated in this work.

This finding emphasizes the potential necessity of mechanical support, such as trays, in applications involving elevated temperatures.

It should be noted that this is a relatively unexplored area, as to our knowledge, very few if any studies have probed the tensile strength of composite PCMs at high temperatures provoking their transition to a liquid state.

3.2. Experimental thermal energy storage device results

The charging process for the TES tank was carried out with a consistent volumetric flow rate of 0.03167 m^3/s. The flow rate was measured using a flowmeter at the outlet of the tank. Depending on the temperature of the air at the inlet, this translates to a mass flow rate ranging between 0.030 and 0.021 kg/s. The set point of the heating element was established at 430 °C, though the heater could not deliver an inlet temperature exceeding 410 °C at this flow rate due the given 10 kW power limitations.

The complete charging process lasted for a total of 9 h during the course of a day. Prior to initiating the first charging process, the tank was maintained at 150 °C for 48 h to eliminate trapped moisture and organic contaminants. Significant water content was detected in the tank, confirmed by a high humidity in the outlet stream, a by-product of the firing process. The latter was not conducted long enough to fully evaporate all the water content used for enhancing green density.

Looking at the data, it appears that the charging process progresses in a way that one would generally expect, considering the principles of heat transfer. The thermocouples positioned at the upper parts of the tank (T2, T3, and T4) reach higher temperatures faster than the ones situated lower down (T5, T6, T8, and T9), as expected in a top-down charging process (Fig. 9).

Analysing the data from T2L, where the PCM is NaNO$_3$ with a higher melting point of 308 °C, one can observe that the temperature surpasses this melting point at approximately the 2.8-h mark, indicating the onset of the phase change process. This is followed by a more gradual temperature increase, reflecting the endothermic nature of the phase change process and the inherent thermal resistance of the material at its temperature approaches that of T1.

On the other hand, T3, T4, and T5L, where SS based CPCMs are located, with a melting point of 218 °C, show that the phase change initiation occurs at different stages of the charging process. More specifically, T3 begins this process around the 4.5-h mark, T4 at 5.4 h, and T5L at 6.6 h (Fig. 9). The delay in the phase change initiation for each of these thermocouples indicates a well-controlled and step-wise execution of the charging process.

The data from the thermocouples at T6, T8, and T9, located closer to the bottom of the tank, record a slower rise in the temperature over time. These temperatures never reach the melting point of the SS within the given timeframe. The limited duration of the charging process can be attributed to the fact that it required on-site supervision during working hours, due to the high voltage of the heater.

Apart from a vertical investigation of the thermal profile, a radial one is also conducted. During the charging phase, the hot air enters from the top of the tank. The data shows that T2L heats up faster than T2M and T2S, suggesting that the heat transfer to the core (T2L) is more effective than at the sides (T2S). This is likely because the hot air first encounters the central part of the tank, where T2L is located. However, the flow resistance at the centre might be higher due to a denser packing or possible obstructions, which slows the air flow, increasing its residence time, and thus its opportunity to transfer heat locally to the surrounding CPCM. As a result, T2L records higher temperatures compared to T2S and T2M (Fig. 9). This pattern, however, wasn't consistent for T5 as T5S exceeded T5M and T5L, indicating a redirection of a more substantial air portion towards the side of the tank between these points. Similar behaviour was observed at T8. This could result from multiple combined factors such as geometrical inconsistencies in the tank or variations in the packing arrangement, which might have created zones of lower flow
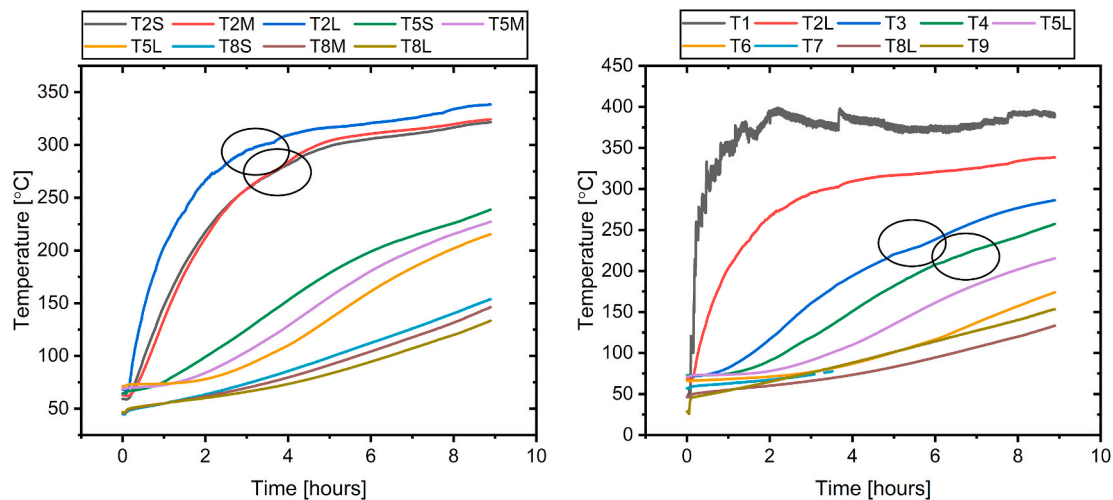
Fig. 9. Thermocouple readings during charging at various positions of the tank. Left: Multiple series, positioned at the centre of the tank, the edge and in between. Right: Single series, positioned only at the middle of the tank.

resistance resulting in an uneven flow distribution. Overall, these radial temperature discrepancies were substantial at the start of the charging process but were nearly identical later on, particularly for T2 thermocouples, signifying that the tank's top layers had thermally equilibrated.

It's important to note that the thermocouples weren't positioned inside the pellets, although in some occasions where in contact with them or accompanying trays and therefore mostly reflect the air temperature at the specific tank positions.

The efficiency during charging, was found to be 79.5 ± 1.83%. This is within the typically reported range in the literature and signifies a reasonable level of efficiency. Notably, this charging efficiency is derived from an average of three independent runs. An 'independent run' is characterized by the process where the TES tank is initially brought to equilibrium with the ambient temperature of approximately 25 °C, followed by initiation of the charging process.

The inefficiencies in TES systems are typically a result of heat losses, and poor heat transfer [64]. The ideal porosity for packed bed TES systems ranges between 30 and 40 % [64]. Higher porosity, such as observed in this case, leads to inefficient heat transfer [64]. Conversely, lower porosity often results in pressure drops, causing backflow, flow reduction, and inefficient heat delivery. Despite structural limitations preventing us from achieving the ideal porosity, the resultant value was
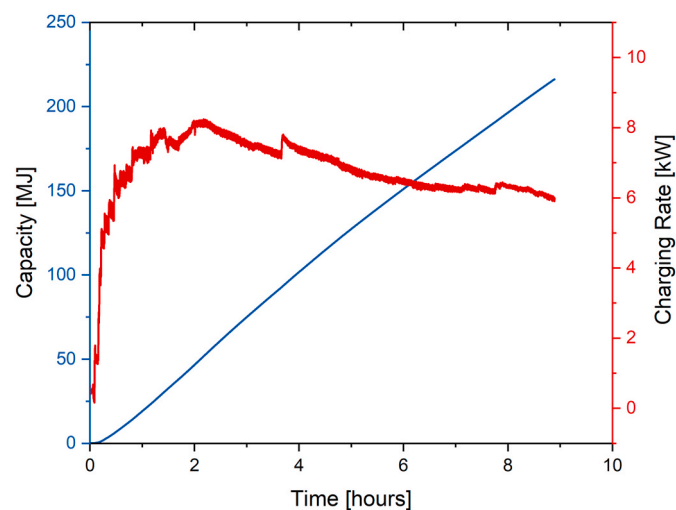
satisfactory.

Next, the two critical parameters in PBLHS performance, namely, the charging capacity (MJ) and the instantaneous charging rate (kW) are investigated.

Analysing the data, it's evident that the charging capacity increases linearly with time. The consistency of this trend, with no signs of levelling off, indicates that the system is not yet approaching thermal equilibrium with its surroundings (Fig. 10).

The instantaneous charging rate exhibits a more intricate pattern. During the initial stages of the charging process, there is a sharp increase in the charging rate. This initial increase is likely due to the larger temperature gradient at the start of the process, where the packed bed is at a lower temperature compared to the charging source. As a result, a higher rate of heat transfer is possible, leading to a faster rate of energy absorption. This concept is anchored on the Fourier's law of heat conduction, which states that the rate of heat transfer per unit area is directly proportional to the temperature gradient in a material.

In terms of the overall behaviour of the device during the charging process, the data suggests that the device charges most efficiently during the first 150 min or so, where the instantaneous charging rate is steadily increasing (Fig. 10). Beyond this point, while the device continues to accumulate charge, it does so at a decreasing rate. This information can be crucial when considering the use of this device in applications where rapid charging is important.

The charging rate starts to decline after peaking at 148.4 min (9.6 kW). This is a direct indication of the device approaching thermal equilibrium. As the temperature difference between the packed bed and the heat source decreases, the heat transfer rate also slows down. Additionally, the various thermal losses, such as conductive and convective, become more significant, further contributing to the decrease in the net heat transfer rate.

The discharging process operates inversely to the charging process. Here, the fan is connected to the bottom of the tank, and the airflow is reversed to optimize the heat transfer. Despite taking over a full day to complete, discharging sustains an outlet temperature (T1) of around 37 °C after 26 h of continuous discharge flow (Fig. 11). This demonstrates the device's effectiveness for space heating applications over extended periods.

An apparent observation during discharging is the clear pattern of thermal stratification that occurs from the outlet top (T1) to the inlet bottom (T9) at any given time. This is demonstrated by the uniformly decreasing temperature values from T1 to T9. This feature enhances the efficiency during the discharging process by allowing the extraction of heat from the hottest part of the system first, therefore extending the
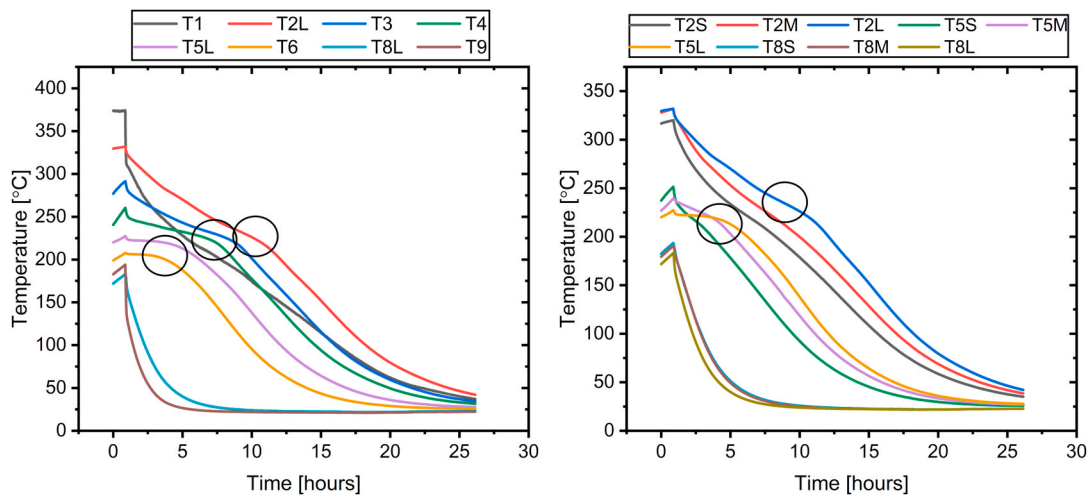

Fig. 10. The relationship between instantaneous charging rate and time (right) as well as charging capacity and time (left).

Fig. 11. Thermocouple readings at various positions of the tank. Right: Multiple series, positioned at the centre of the tank, the edge and in between. Left: Single series, positioned only at the middle of the tank.

useful period of heat delivery (Fig. 11). Interestingly, the thermocouples positioned at various points in the device show a time lag in their responses. The topmost thermocouple, T1, exhibits a rapid decrease in temperature compared to those positioned lower, aligning with the expectation that heat is discharged from the top and gradually works its way towards the bottom.

Apart from the axial thermocouples, there is also data available from the radial ones. Looking at the data for T2S, T2M, and T2L, representing the short, middle, and long axial positions, one can observe that T2S, being closer to the tank wall, tends cools down faster due to the high thermal conductivity of the tank material. Conversely, T2L, experiences a slower cooling, maintaining higher temperatures for longer periods. When comparing data from T5 and T8, positioned in the middle and the bottom of the tank respectively, similar patterns emerge. The thermocouples at the S positions tend to cool faster than those at the L positions.

With regards to flow direction, the temperature pattern, at T5 aligns more with the flow observed during charging, with T5S exceeding T5M and T5L. However, an aberration in this pattern is seen at T2, where T2L exhibits higher temperatures than T2S during discharging. In this scenario, since the flow is moving in the opposite direction, the air primarily follows the path of least resistance, which is along the side of the tank, effectively cooling T2S more than T2M and T2L. This suggests that during discharging, the cooled air may be bypassing the denser or obstructed regions of the device. These regions of higher flow resistance deter the cooled air from flowing uniformly, forcing a larger fraction of it towards the tank's walls, resulting in less effective cooling at the tank's core.

These variations in temperature and flow patterns suggest a complex thermal and flow dynamic. Understanding these intricacies is crucial for optimizing the design and the operation of the TES system.

Another interesting point is the evident phase change plateaus during discharging, which demonstrate a temporal offset. The offset corresponds to the time required for each layer to undergo phase change. As the heat from the top layers is depleted, the phase change occurs progressively at higher positions in the tank. Overall, the discharge temperature (T1) primarily aligns with the median temperatures at T3 and T4, located at the upper-middle position of the tank.

While T2L does display a plateau at approximately 240 °C, it's essential to highlight that this isn't indicative of NaNO₃'s phase change. Instead, the gradient variation in the T2 curves before and after this plateau suggests that the NaNO₃ underwent its phase change around its melting point of 308 °C during the earlier stages of discharge. This phase transition in the T2 region occurred in parallel with the phase change observed in the zones dominated by Solar Salt (T3 to T6).

The observed plateau at T2L, closer to the melting point of Solar Salt (SS) than to NaNO₃, can be attributed to the significant portion of the tank still undergoing phase transition at this temperature range. With the flow moving from the bottom to the top, it's plausible that the heat associated with this phase change in the lower regions is pushed upwards, aligning with the temperature regime of the T2 zone. These complex thermal interactions of cascade TES systems highlight the layers of complexity and underscore the necessity of a thorough understanding of the heat transfer processes in such systems.

The discharge efficiency of the TES device is calculated as 86.2 ± 2.3%. Like the charging efficiency, this is obtained as the average of the two independent runs. Finally, the total efficiency is found to be 68.51 ± 2.11%. Overall, the efficiency is somewhat lower than what is reported in the literature. This means there is substantial room for improvement in the form of CPCM geometry optimization and addition of more PCM materials into the mix. Another significant drawback is the metal frame supporting the tanks, which heats up along with the CPCM and can reach temperatures up to 180 °C near the joints. Replacing the metal frame with a low-density ceramic jacket would likely reduce thermal losses and enhance efficiency. However, such a modification could compromise the device's mobility, a crucial factor considering applications in industrial settings.
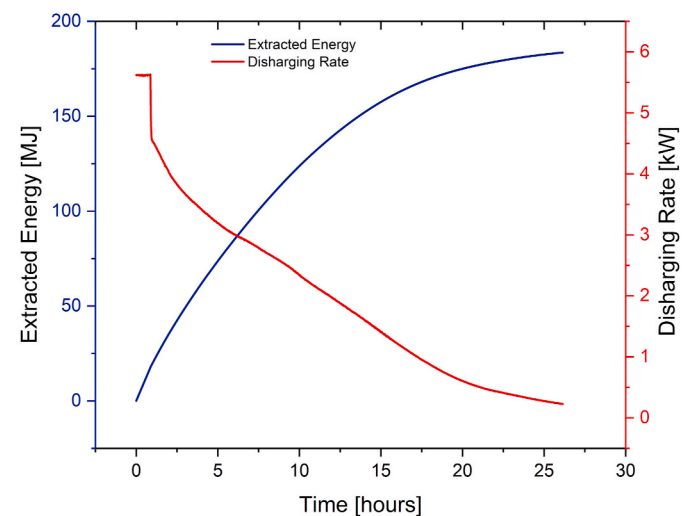

Fig. 12. The relationship between instantaneous discharging rate (right) and extracted energy (left) with time during discharging.

Mirroring the approach for the charging process, the discharging characteristics of the TES device are evaluated through two critical parameters: the extracted energy, and the instantaneous discharging rate (Fig. 12).

The extracted energy, observed over a time span of 25.1 h, demonstrates a consistent decline. This trend indicates that the stored energy within the system is progressively being depleted.

The instantaneous discharging rate data offers another perspective on the system's behavior. Initiating at rate of 5.6 kW at the 0.6-h mark, there is a clear and steady decline, reaching 0.3 kW by the 24.7-h mark. This underscores the system's reduced ability to discharge energy as time progresses. This is due to the decreasing temperature gradient between the packed bed and its surroundings as well as inherent thermal losses in the system.

Apart from the standard charging/discharging experiments, a further charging process, identical in the methodology to the one described above, was executed. This was immediately followed by a procedure commonly referred to as "free cooling", where the tank was placed in an idle state for an extended duration. Both the inlet and the outlet were sealed, effectively isolating the internal thermal energy from the external environment. The evolution of temperature within the tank was recorded overnight.

This free cooling experiment was intentionally designed to mirror the real-world scenarios in various industrial settings where heat generated and stored during one operational cycle, such as during a daytime shift, could potentially be utilized at a later time. For instance, the stored thermal energy could be harnessed for space heating purposes on subsequent days. By isolating the thermal energy within the tank and observing its dispersion over time, insights were obtained regarding heat retention and the dynamics of heat transfer within the tank during the periods of inactivity.

At the onset of the free cooling period, T2L exhibited the highest temperature of 336.5 °C, whereas T9 demonstrated the lowest at 135.4 °C (Fig. 13). With the progression of time, a reduction in temperature was noticed across all the points, reflecting a thermodynamically predictable process of heat dissipation from the tank towards its cooler surroundings.

A more detailed look at the data reveals that the top of the tank (T1) underwent the most accelerated rate of cooling, indicative of the direct proportionality between the rate of heat loss and the difference in temperature between the system and its environment. In contrast, the lower sections experienced a slower cooling rate, owing to a smaller initial temperature difference with the surrounding environment and likely superior insulation due to less direct exposure.

Interestingly, there are instances of slight temperature elevations at certain points (T4, T5L, T6, and T8L) throughout the free cooling period.

These can be attributed to the redistribution of residual heat from warmer to cooler areas within the tank, in accordance with the principle of thermal equilibrium.

The free cooling experiment also tracked radial temperature variations at three distinct levels within the tank: T2, T5, and T8. The obtained data demonstrated that the temperature changes within the tank were not solely dependent on the vertical position but were also influenced by the radial distance from the tank wall.

At the onset of the free cooling phase, the outer edges of the tank (S positions) registered slightly higher temperatures compared to the middle (M) and the innermost (L) areas. For example, at T2, the outer edge (T2S) recorded a temperature of 306.9 °C, while the medium (T2M) and the innermost (T2L) positions registered 305.7 °C and 295.8 °C, respectively. This observation can be attributed to the higher initial heat exposure experienced by the outer sections of the tank during the charging phase.

As the free cooling phase progressed, temperatures at all radial positions decreased. Notably, S positions demonstrated a steeper temperature drop compared to the M and L positions. In line with the principles of thermodynamics, the tank wall, having the highest surface area exposed to the environment, accounted for the majority of the heat losses. This with reduced flow obstructions, compared to the M and L positions, further accelerated the rate of heat loss to the surrounding environment. This insight underscores the importance of effective insulation strategies for TES loss minimization during idle periods.

4. Conclusions

This research has demonstrated the potential of waste foundry sand composite phase change materials (WFS-CPCMs) in thermal energy storage (TES) and waste heat recovery (WHR). The study has shown that the Packed Bed Latent Heat Storage (PBLHS) unit, based on WFS-CPCMs, can effectively capture and reuse the waste heat from industrial processes, particularly those with temperatures ranging between 200 and 450 °C. The findings suggest that this approach could offer a sustainable and potentially cost-effective solution to energy efficiency challenges in the foundation industries. The key conclusions are as follows:

Material Characterization.

- The energy storage density of the investigated CPCMs is significant, with $NaNO_3$ containg samples reaching 542.0 ± 8.3 kJ/kg, and SS containing samples exhibiting an energy density of 516.0 ± 4.5 kJ/kg. These findings surpass previous state-of-the-art research involving waste, underscoring the advanced performance
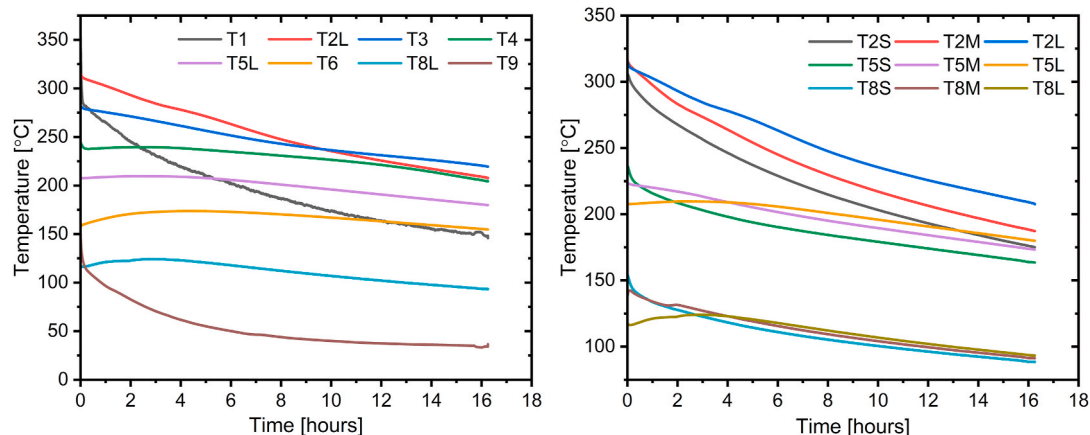

Fig. 13. Thermocouple readings at various positions of the tank during free cooling. Right: Multiple series, positioned at the centre of the tank, the edge and in between. Left: Single series, positioned only at the middle of the tank.

capabilities of the investigated CPCMs for potential application in high-performance TES systems.

- The tensile strength of the composites decreases significantly at elevated temperatures, highlighting the need for mechanical support, such as trays, in high-temperature applications. This is due to the phase change of the salts from a solid to a liquid state, which negatively impacts the structural integrity and mechanical stability of the materials.
- The thermal conductivity of the composites, a critical parameter in CPCM design, decreases with increasing temperature. The SS composite averages 1.17 ± 0.72 W/mK across the investigated temperature range, while the NaNO$_3$ composite averages 1.45 W/mK. The encapsulation of the PCMs within ceramic matrices significantly enhances the thermal conductivity of the resulting TES materials.

Experimental Setup.

- The charging process is well-controlled, with the upper thermocouples heating faster than the lower ones, indicating a step-wise execution. This is also reflected through the phase change initiation, which occurs at different stages for each thermocouple, reflecting the material's inherent thermal resistance.
- The charging efficiency was found to be $79.51 \pm 1.83\%$, within the typically reported range, indicating a reasonable level of efficiency despite potential heat losses due to the gaps in insulation and poor heat transfer due to possible flow obstructions.
- The discharge efficiency of the TES device is found to be $86.20 \pm 2.30\%$, leading to a total efficiency of $68.51 \pm 2.11\%$. This is somewhat lower than what is reported in the literature, indicating a room for improvement through optimization of the CPCM's geometry, addition of more PCMs with different melting points, and potential modifications to reduce the thermal losses, such as the use of a less thermally conductive supporting material for the TES tank.
- The discharging process reveals distinct differences in flow patterns and temperature distribution within the tank. The thermocouples closer to the tank wall cool faster due to faster heat transfer, while those in the middle maintain higher temperatures for longer periods. This suggests a complex thermal and flow dynamic within the tank. Understanding this could lead to further optimization of the TES system design and operation.
- The system is also investigated during a free cooling, where the tank is placed in an idle state for 12h, after charging. No considerable losses are observed during that period, suggesting that the proposed setup can be effectively used for intraday applications.

In conclusion, this study offers a significant contribution to sustainable energy solutions by demonstrating the potential of waste foundry sand (WFS) in thermal energy storage systems. The use of WFS not only provides a cost-effective and sustainable alternative to natural sand but also highlights the potential use of waste materials in high-performance applications. The findings underscore the importance of understanding and optimizing material properties and system design to enhance charging and discharging efficiencies, as well as thermal energy retention during idle periods. This research paves the way for further advancements in the field of thermal energy storage, emphasizing the role of sustainable and innovative materials in the future of energy solutions.

CRediT authorship contribution statement

Abdalqader Ahmad: Data curation, Formal analysis, Investigation, Methodology. **Argyrios Anagnostopoulos:** Conceptualization, Data curation, Formal analysis, Funding acquisition, Investigation, Methodology, Project administration, Resources, Supervision, Validation, Visualization, Writing – original draft, Writing – review & editing. **M. Elena Navarro:** Conceptualization, Formal analysis, Investigation, Methodology, Project administration, Validation, Visualization, Writing – original draft. **Yelaman Maksum:** Formal analysis, Investigation, Methodology. **Shivangi Sharma:** Formal analysis, Investigation, Methodology, Writing – original draft. **Yulong Ding:** Conceptualization, Resources, Software, Supervision.

Declaration of competing interest

The authors declare that they have no known competing financial interests or personal relationships that could have appeared to influence the work reported in this paper.

Data availability

Data will be made available on request.

Acknowledgements

References

[1] Ellabban O, Abu-Rub H, Blaabjerg F. Renewable energy resources: current status, future prospects and their enabling technology. Renew Sustain Energy Rev 2014; 39. https://doi.org/10.1016/j.rser.2014.07.113.

[2] European Commission. Energy Strategy. 2030. 2024. Europa 2016.

[3] Global IEA. Energy review: CO2 emissions in 2020. Glob Energy Rev 2021.

[4] Malinauskaite J, Jouhara H, Ahmad L, Milani M, Montorsi L, Venturelli M. Energy efficiency in industry: EU and national policies in Italy and the UK. Energy 2019; 172. https://doi.org/10.1016/j.energy.2019.01.130.

[5] Agathokleous R, Bianchi G, Panayiotou G, Aresti L, Argyrou MC, Georgiou GS, et al. Waste Heat Recovery in the EU industry and proposed new technologies. Energy Proc 2019;161:489–96. https://doi.org/10.1016/j.egypro.2019.02.064.

[6] Jouhara H, Khordehgah N, Almahmoud S, Delpech B, Chauhan A, Tassou SA. Waste heat recovery technologies and applications. Therm Sci Eng Prog 2018;6: 268–89. https://doi.org/10.1016/j.tsep.2018.04.017.

[7] Miró L, Gasia J, Cabeza LF. Thermal energy storage (TES) for industrial waste heat (IWH) recovery: a review. Appl Energy 2016;179. https://doi.org/10.1016/j.apenergy.2016.06.147.

[8] Fernández AI, Barreneche C, Miró L, Brückner S, Cabeza LF, Fernández AI, et al. Waste heat recovery using thermal energy storage. Adv. Therm. Energy Storage Syst. 2021. https://doi.org/10.1016/b978-0-12-819885-8.00022-x.

[9] Palacios A, Barreneche C, Navarro ME, Ding Y. Thermal energy storage technologies for concentrated solar power – a review from a materials perspective. Renew Energy 2019. https://doi.org/10.1016/j.renene.2019.10.127.

[10] Jouhara H, Żabnieńska-Góra A, Khordehgah N, Ahmad D, Lipinski T. Latent thermal energy storage technologies and applications: a review. Int J Thermofluids 2020:5–6. https://doi.org/10.1016/j.ijft.2020.100039.

[11] Jiang F, Zhang L, She X, Li C, Cang D, Liu X, et al. Skeleton materials for shape-stabilization of high temperature salts based phase change materials: a critical review. Renew Sustain Energy Rev 2020;119:109539. https://doi.org/10.1016/j.rser.2019.109539.

[12] Anagnostopoulos A, Navarro ME, Stefanidou M, Ding Y, Gaidajis G. Red mud-molten salt composites for medium-high temperature thermal energy storage and waste heat recovery applications. J Hazard Mater 2021:413. https://doi.org/10.1016/j.jhazmat.2021.125407.

[13] Anagnostopoulos A, Navarro M, Ahmad A, Ding Y, Gaidajis G. Valorization of phosphogypsum as a thermal energy storage material for low temperature applications. J Clean Prod 2022;342:130839. https://doi.org/10.1016/J.JCLEPRO.2022.130839.

[14] Abdelsalam MY, Teamah HM, Lightstone MF, Cotton JS. Hybrid thermal energy storage with phase change materials for solar domestic hot water applications: direct versus indirect heat exchange systems. Renew Energy 2020;147. https://doi.org/10.1016/j.renene.2019.08.121.

[15] Siddique R, Noumowe A. Utilization of spent foundry sand in controlled low-strength materials and concrete. Resour Conserv Recycl 2008;53. https://doi.org/10.1016/j.resconrec.2008.09.007.

[16] Mavroulidou M, Lawrence D. Can waste foundry sand fully replace structural concrete sand? J Mater Cycles Waste Manag 2019;21:594–605. https://doi.org/10.1007/S10163-018-00821-1/FIGURES/8.

[17] Sabour MR, Derhamjani G, Akbari M, Hatami AM. Global trends and status in waste foundry sand management research during the years 1971-2020: a systematic analysis. Environ Sci Pollut Res 2021;28:37312–21. https://doi.org/10.1007/S11356-021-13251-8/FIGURES/7.

[18] Guney Y, Sari YD, Yalcin M, Tuncan A, Donmez S. Re-usage of waste foundry sand in high-strength concrete. Waste Manag 2010;30:1705–13. https://doi.org/10.1016/J.WASMAN.2010.02.018.

[19] Siddique R, Singh G. Utilization of waste foundry sand (WFS) in concrete manufacturing. Resour Conserv Recycl 2011;55. https://doi.org/10.1016/j.resconrec.2011.05.001.

[20] Peris B, Navarro-Esbrí J, Molés F, Mota-Babiloni A. Experimental study of an ORC (organic Rankine cycle) for low grade waste heat recovery in a ceramic industry. Energy 2015. https://doi.org/10.1016/j.energy.2015.03.065.

[21] Felix Regin A, Solanki SC, Saini JS. An analysis of a packed bed latent heat thermal energy storage system using PCM capsules: numerical investigation. Renew Energy 2009;34:1765–73. https://doi.org/10.1016/J.RENENE.2008.12.012.

[22] Gautam A, Saini RP. A review on technical, applications and economic aspect of packed bed solar thermal energy storage system. J Energy Storage 2020;27:101046. https://doi.org/10.1016/J.EST.2019.101046.

[23] Medrano M, Gil A, Martorell I, Potau X, Cabeza LF. State of the art on high-temperature thermal energy storage for power generation. Part 2—case studies. Renew Sustain Energy Rev 2010;14:56–72. https://doi.org/10.1016/J.RSER.2009.07.036.

[24] He X, Qiu J, Wang W, Hou Y, Ayyub M, Shuai Y. A review on numerical simulation, optimization design and applications of packed-bed latent thermal energy storage system with spherical capsules. J Energy Storage 2022;51:104555. https://doi.org/10.1016/J.EST.2022.104555.

[25] Ananthanarayanan V, Sahai Y, Mobley CE, Rapp RA. Modeling of fixed bed heat storage units utilizing phase change materials. Metall Trans B 1987;18:339–46. https://doi.org/10.1007/BF02656152/METRICS.

[26] Beasley DE, Ramanarayanan C, Torab H. Thermal response of a packed bed of spheres containing a phase-change material. Int J Energy Res 1989;13:253–65. https://doi.org/10.1002/ER.4440130302.

[27] Yagi J, Akiyama T. Storage of thermal energy for effective use of waste heat from industries. J Mater Process Technol 1995;48:793–804. https://doi.org/10.1016/0924-0136(94)01723-E.

[28] Ismail KAR, Henríquez JR. Numerical and experimental study of spherical capsules packed bed latent heat storage system. Appl Therm Eng 2002;22:1705–16. https://doi.org/10.1016/S1359-4311(02)00080-7.

[29] Nallusamy N, Sampath S, Velraj R. Experimental investigation on a combined sensible and latent heat storage system integrated with constant/varying (solar) heat sources. Renew Energy 2007;32:1206–27. https://doi.org/10.1016/J.RENENE.2006.04.015.

[30] Wu M, Xu C, He YL. Dynamic thermal performance analysis of a molten-salt packed-bed thermal energy storage system using PCM capsules. Appl Energy 2014;121:184–95. https://doi.org/10.1016/J.APENERGY.2014.01.085.

[31] Bellan S, Alam TE, González-Aguilar J, Romero M, Rahman MM, Goswami DY, et al. Numerical and experimental studies on heat transfer characteristics of thermal energy storage system packed with molten salt PCM capsules. Appl Therm Eng 2015;90. https://doi.org/10.1016/j.applthermaleng.2015.07.056.

[32] Bhagat K, Saha SK. Numerical analysis of latent heat thermal energy storage using encapsulated phase change material for solar thermal power plant. Renew Energy 2016;95. https://doi.org/10.1016/j.renene.2016.04.018.

[33] Wu M, Xu C, He Y. Cyclic behaviors of the molten-salt packed-bed thermal storage system filled with cascaded phase change material capsules. Appl Therm Eng 2016;93. https://doi.org/10.1016/j.applthermaleng.2015.10.014.

[34] Zhao B chen, Cheng M song, Liu C, Dai Z min. Cyclic thermal characterization of a molten-salt packed-bed thermal energy storage for concentrating solar power. Appl Energy 2017;195. https://doi.org/10.1016/j.apenergy.2017.03.110.

[35] Zhao B chen, Cheng M song, Liu C, Dai Z min. System-level performance optimization of molten-salt packed-bed thermal energy storage for concentrating solar power. Appl Energy 2018;226. https://doi.org/10.1016/j.apenergy.2018.05.081.

[36] Li MJ, Jin B, Ma Z, Yuan F. Experimental and numerical study on the performance of a new high-temperature packed-bed thermal energy storage system with macroencapsulation of molten salt phase change material. Appl Energy 2018;221. https://doi.org/10.1016/j.apenergy.2018.03.156.

[37] Liao Z, Xu C, Ren Y, Gao F, Ju X, Du X. A novel effective thermal conductivity correlation of the PCM melting in spherical PCM encapsulation for the packed bed TES system. Appl Therm Eng 2018;135. https://doi.org/10.1016/j.applthermaleng.2018.02.048.

[38] Liu HB, Zhao CY. Effect of radial porosity oscillation on the thermal performance of packed bed latent heat storage. Engineering 2021;7. https://doi.org/10.1016/j.eng.2020.05.020.

[39] Li C, Li Q, Ding Y. Investigation on the thermal performance of a high temperature packed bed thermal energy storage system containing carbonate salt based composite phase change materials. Appl Energy 2019;247. https://doi.org/10.1016/j.apenergy.2019.04.031.

[40] Saha SK, Das RB. Exergetic and performance analyses of two-layered packed bed latent heat thermal energy storage system. Int J Energy Res 2020;44. https://doi.org/10.1002/er.5081.

[41] Yang X, Cai Z, Zuo Y. Heat transfer performance of a storage system of molten-salt thermocline-packed bed. J Renew Sustain Energy 2020;12. https://doi.org/10.1063/5.0021299.

[42] Wang W, He X, Hou Y, Qiu J, Han D, Shuai Y. Thermal performance analysis of packed-bed thermal energy storage with radial gradient arrangement for phase change materials. Renew Energy 2021;173. https://doi.org/10.1016/j.renene.2021.04.032.

[43] Sau GS, Tripi V, Tizzoni AC, Liberatore R, Mansi E, Spadoni A, et al. High-temperature chloride-carbonate phase change material: thermal performances and modelling of a packed bed storage system for concentrating solar power plants. Energies 2021;14. https://doi.org/10.3390/en14175339.

[44] Nekoonam S, Ghasempour R. Modeling and optimization of a thermal energy storage unit with cascaded PCM capsules in connection to a solar collector. Sustain Energy Technol Assessments 2022;52. https://doi.org/10.1016/j.seta.2022.102197.

[45] Erregueragui Z, Tizliouine A, Omari LEH, Chafi M. Cost performance of encapsulated phase change material-based thermal energy storage systems. Int J Low Carbon Technol 2022;17. https://doi.org/10.1093/ijlct/ctac109.

[46] ElsS ELSihy, Xu C, Du X. Cyclic performance of cascaded latent heat thermocline energy storage systems for high-temperature applications. Energy 2022;239. https://doi.org/10.1016/j.energy.2021.122229.

[47] Wang W, He X, Shuai Y, Qiu J, Hou Y, Pan Q. Experimental study on thermal performance of a novel medium-high temperature packed-bed latent heat storage system containing binary nitrate. Appl Energy 2022;309. https://doi.org/10.1016/j.apenergy.2021.118433.

[48] Manente G, Ding Y, Sciacovelli A. A structured procedure for the selection of thermal energy storage options for utilization and conversion of industrial waste heat. J Energy Storage 2022;51. https://doi.org/10.1016/j.est.2022.104411.

[49] He X, Qiu J, Wang W, Hou Y, Ayyub M, Shuai Y. Optimization design and performance investigation on the cascaded packed-bed thermal energy storage system with spherical capsules. Appl Therm Eng 2023;225. https://doi.org/10.1016/j.applthermaleng.2023.120241.

[50] Navarro ME, Trujillo AP, Jiang Z, Jin Y, Zhang Y, Ding Y. Manufacture of Thermal Energy Storage Materials 2021;7. https://doi.org/10.1039/9781788019842-00121. 121–90.

[51] O'Neill MJ. Measurement of specific heat functions by differential scanning Calorimetry. Anal Chem 1966;38. https://doi.org/10.1021/ac60242a011.

[52] Bashiri Mousavi S, Adib M, Soltani M, Razmi AR, Nathwani J. Transient thermodynamic modeling and economic analysis of an adiabatic compressed air energy storage (A-CAES) based on cascade packed bed thermal energy storage with encapsulated phase change materials. Energy Convers Manag 2021;243. https://doi.org/10.1016/j.enconman.2021.114379.

[53] Mao Q, Zhang Y. Thermal energy storage performance of a three-PCM cascade tank in a high-temperature packed bed system. Renew Energy 2020;152. https://doi.org/10.1016/j.renene.2020.01.051.

[54] Benyahia F, O'Neill KE. Enhanced voidage correlations for packed beds of various particle shapes and sizes. Part Sci Technol 2005;23. https://doi.org/10.1080/02726350590922242.

[55] Agalit H, Zari N, Maalmi M, Maaroufi M. Numerical investigations of high temperature packed bed TES systems used in hybrid solar tower power plants. Sol Energy 2015;122. https://doi.org/10.1016/j.solener.2015.09.032.

[56] Holman JP. Experimental methods for engineers, vol. 9; 2012.

[57] Anagnostopoulos A, Navarro ME, Ding Y. Microstructural improvement of solar salt based MgO composites through surface tension/wettability modification with SiO2 nanoparticles. Sol Energy Mater Sol Cells 2022;238:111577. https://doi.org/10.1016/J.SOLMAT.2022.111577.

[58] Lomonacoa A, Haillot D, Pernot E, Franquet E, Bédécrats JP. Thermal characterization of sodium nitrate - sodium nitrite compounds for thermal storage applications. ECOS 2015 - 28th Int. Conf. Effic. Cost, Optim. Simul. Environ. Impact Energy Syst. 2015.

[59] Xu G, Leng G, Yang C, Qin Y, Wu Y, Chen H, et al. Sodium nitrate – diatomite composite materials for thermal energy storage. Sol Energy 2017;146:494–502. https://doi.org/10.1016/j.solener.2017.03.003.

[60] Mitran R-A, Lincu D, Buhǎlţeanu L, Berger D, Matei C. Shape-stabilized phase change materials using molten NaNO3 – KNO3 eutectic and mesoporous silica matrices. Sol Energy Mater Sol Cells 2020;215:110644. https://doi.org/10.1016/j.solmat.2020.110644.

[61] Yang H, Zhang W, Zhu Y, Shao Y, Shao Y, Zhang X. Preparation and characterisation of sodium nitrate/stone-sawing mud shape-stabilized phase change materials for medium-high temperature thermal energy storage. J Energy Storage 2022;56:106047. https://doi.org/10.1016/J.EST.2022.106047.

[62] Pia G, Sanna U. An intermingled fractal units model to evaluate pore size distribution influence on thermal conductivity values in porous materials. Appl Therm Eng 2014;65. https://doi.org/10.1016/j.applthermaleng.2014.01.037.

[63] Anagnostopoulos A, Alexiadis A, Ding Y. Molecular dynamics simulation of solar salt (NaNO3-KNO3) mixtures. Sol Energy Mater Sol Cells 2019;200:109897. https://doi.org/10.1016/j.solmat.2019.04.019.

[64] Yoo J, Yoon SJ, O'brien TE, Frick KL, O'brien JE, Sabharwall P, et al. Design optimization study on the single tank packed bed thermal energy storage system. Int. Top. Meet. Adv. Therm. Hydraul. ATH 2018 - Embed. Top. Meet. 2018.